8

ANALYSIS OF FINITE SIZED CONDUCTING PATCHES IN MULTILAYER MEDIA USING THE CG-FFT METHOD AND DISCRETIZING GREEN'S FUNCTION IN THE SPECTRAL DOMAIN

E. Gago and M. F. Cátedra

8.1 Introduction

Numerical techniques to analyze conducting surfaces in multilayer media (see Fig. 8.1) are required for the design of flat structures such as microstrip antennas, microwave monolithic integrated circuits, etc, at microwave and higher frequencies. Surveys of numerical techniques to analyze these structures can be found in [1]-[3].

One of these techniques is the Moment Method, (MM), [4]-[6], that has the advantage of being a rigorous method (without assumptions for the current or field behaviors) and is able to treat arbitrarily shaped conducting patches. The disadvantages of MM are well known: the CPU-time and matrix storage requirements limit seriously the scope of MM to electrically small problems.

Recently a new method, the Conjugate Gradient-Fast Fourier Transform Method (CG-FFT), [3], [7]-[13], is being developed that

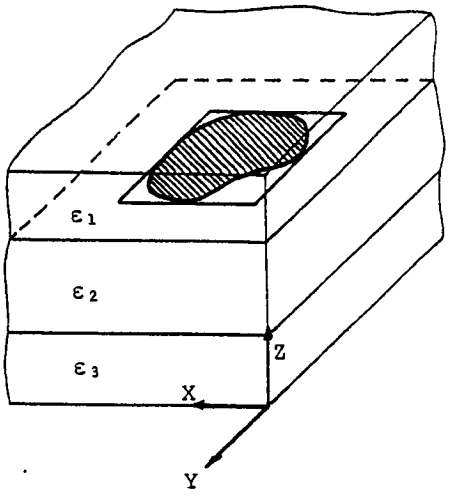

Figure 8.1 Arbitrary conducting surface in multilayer media.

appears to be more efficient than MM for some problems. The two methods have several common features. With them, problems are usually treated solving an Integral Equation, (IE), where the unknown function is the induced current. This IE is sampled by expanding the current in terms of basis functions and weight the fields with some set of testing functions.

The main difference between the two methods is that using CG-FFT the computational efficiency is largely improved in CPU time and in storage memory requirements, due to performing the convolutions of the IE by means of FFT's. To obtain this improvement the IE must be of convolution nature and both the basis and testing function sets must be obtained by shifting at regular points a single function. MM is more flexible and does not have these restrictions for the IE and for the basis and testing functions. As can be seen later in the chapter, metallic patches in multilayer media is one of the problems for which a very efficient and accurate use of CG-FFT can be made.

The CG-FFT method is applied to solve problems formulated in terms of operator equations such as

$$LI = Y \tag{1}$$

In our problem (1) is an IE, L is an integrodifferential operator, I represents the induced current to be computed, and Y is related to the

impressed field. L has a convolution nature. The CG method, [7], requires in each iteration to perform operations like LW or L^aW, where W is a known function and L^a is the adjoint operator of L. In the numerical approach operators L and L^a must be discretized and one of the main difficulties for the CG-FFT method is to obtain the corresponding discrete operators L^D and L^{aD}. Actually the performance of the CG-FFT method depends strongly on the procedure devised to obtain these discrete operators.

Finite-sized problems can be solved by performing all the sampling process in the real domain. A discrete Green's function is obtained from the continuous Green's function by sampling at regular points the fields due to a basis function centered at the origin of coordinates. These fields are weighted with the testing functions prior to the sampling. This technique is useful when in the real domain simple and analytical expressions for Green's functions are available, [9]-[11].

Periodic, infinite-sized problems can be solved by sampling in the spectral domain at regular points the continuous Green's function expression, [12]-[13]. The aliasing due to this sampling is advantageous to take easily into account the periodic behavior of the problem in the real domain. Ripple problems can be avoided taking into account the periodicity in the spectral domain of the discrete operator that appear due to the sampling of the fields in the real domain at regular points, [13].

In this chapter finite-sized patches in multilayer media are analyzed by sampling the Green's function in the spectral domain. For these media Green's functions are of troublesome computation in the real domain, but in the spectral domain they have simple analytical expressions. An extension is made of the CG-FFT scheme for periodic structures given in [13]. Now a modified Green's function is sampled in the spectral domain. This function is periodic in the real domain with a rectangular generating cell of side lengths at least twice those of the rectangle of minimum area that envelopes completely all the patches of the problem. Over the generating cell the modified Green's function can be obtained by windowing the original Green's function for the structure considered, using a function that vanishes at all points outside the generating cell.

The technique described in [13] was for problems formulated in terms of a Mixed–Potential Integral Equation (MPIE). Here, more general IE's are considered. Most of the IE formulations for multilayer

media are not written in terms of MPIE's.

A previous work applying a CG-FFT scheme to multilayer problems is reported in [3]. The paper itself and its references give very few details of the CG-FFT scheme considered. In the present chapter a different CG-FFT scheme is described in detail. It has several new features, mainly the introduction of a modified Green's function and the treatment in the spectral domain of nearly all the computations required to sample the continuous operator. This sampling is done considering rooftops as basis functions and razor-blade functions as testing functions, [10],[16]. Discrete fields in both domains are obtained. The periodic behavior in the spectral domain allows to perform easily all the computations without neglecting high spectral-frequency terms. The results obtained for convergence rates, current distributions and RCS values indicate that the CG-FFT scheme appears to be a very useful method to treat the problem shown in Fig. 8.1.

This chapter is arranged as follows: In part II an Electric Field Integral Equation (EFIE) with a modified Green's function is introduced. This EFIE is discretized in part III using rooftop functions to expand the current and razor-blade functions to weight the fields. The weighted fields are discretized by sampling them with a train of impulse functions. Part III ends with expressions for the sampled fields where nearly all the integrals required to compute the induced fields are expressed in terms of convolutions. These convolutions are computed efficiently by means of FFT's as shown in Part IV. In the spectral domain the induced fields are obtained computing the product of two discrete and periodic functions. One of them is the FFT of the discrete function that forms the coefficients of the expansion of the induced current in terms of rooftops. The other function is obtained from a series, whose terms include values of the Continuous Fourier Transform (CFT) of the modified Green's function. In Part V some details of the evaluation of the modified Green's function are given. Results of current distributions, convergence rates and RCS values for metallic plates and microstrip structures are given in Part VI. All these results have been obtained using the Conjugate Gradient algorithm that appears in [10]. The chapter ends with an Appendix with complete expressions for the discretized operator.

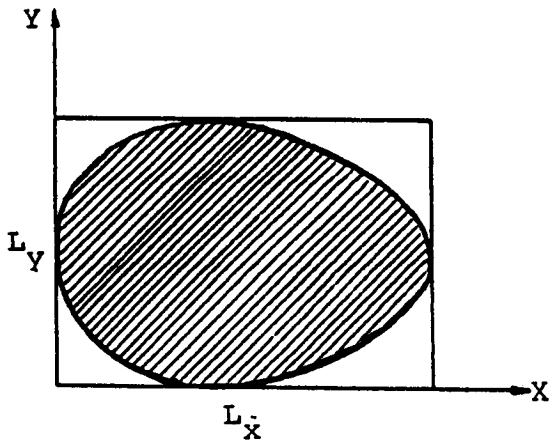

Figure 8.2 Geometry of the arbitrary patch considered. The patch is enclosed by a rectangle of sides L_x and L_y.

8.2 Formulation of the Continuous Operator Equation

Figure 8.2 shows the geometry of an arbitrary flat metallization that is assumed lying in a plane $z = h$. All the metallization is enclosed in a rectangle of area $L_x L_y$.

The induced current on the metallic surface can be obtained by solving the following operator equation

$$\hat{z} \times E^i(r) = \hat{z} \times \int_{S_p} G(r - r')J(r')ds' \qquad \text{for } r \epsilon S_p \tag{2}$$

where E^i is the impressed field, S_p is the metallic surface and G is the dyadic Green's function that relates the electric fields with the surface currents in the plane $z = h$.

Now we define a new dyadic, G^w, that we will call "windowed" Green's function. This function can be obtained from G using

$$G^w(r) = Z(r)G(r) \tag{3}$$

where $Z(r)$ is a function that vanishes for $|x| > L_x$ or $|y| > L_y$. When $Z(r)$ is made equal to the pulse function defined in the table, (2) can be written as follows

$$\hat{z} \times E^i(r) = \hat{z} \times \int_{S_p} G^F(r - r')J(r')ds' \qquad \text{for } r \epsilon S_p \tag{4}$$

WINDOW FUNCTIONS

NAME	REAL DOMAIN (x)	SPECTRAL DOMAIN (k_x)
Pulse	1.	$2\,\frac{\sin(k_x)}{k_x} = 2\,\mathrm{sinc}(k_x/\pi)$
Triangle	$1.- \lvert x\rvert$	$2\,\mathrm{sinc}^2(k_x/\pi)$
Hanning	$\frac{1}{2}\left[1 - \cos(\pi x + 1)\right]$	$\mathrm{sinc}(k_x/\pi) +$ $+ 1/2\,\mathrm{sinc}(k_x/\pi - 1) +$ $+ 1/2\,\mathrm{sinc}(k_x/\pi + 1)$
Welch	$1 - \alpha x^2$	$2(1-\alpha)\,\mathrm{sinc}(k_x/\pi)$ $+ \frac{4\alpha}{k_x^3}\sin(k_x) -$ $- \frac{4\alpha}{k_x^2}\cos(k_x)$

Table Some one-dimensional window functions for the normalized interval (-1.,1.). In this work $\alpha = 1$.

where G^F is a periodic dyadic function defined as

$$G^F = \sum_{m=-\infty}^{\infty} \sum_{n=-\infty}^{\infty} G^w(r - v_{mn}) \tag{5}$$

where

$$v_{mn} = mT_x\hat{x} + nT_y\hat{y} \tag{6}$$

and

$$T_x = 2L_x \tag{7.a}$$

$$T_y = 2L_y \tag{7.b}$$

It can be noticed that G^F has a periodic cell of size T_xT_y. When $Z(r)$ is made equal to a pulse, (2) is satisfied exactly. If $Z(r)$ is made equal to some of the space-limited functions of the table, (2) is only satisfied approximately.

8.3 Discretization of the Operator Equation

To discretize the continuous operator equation of (4) the induced current, J, is expanded in terms of "rooftop" functions, R_x^{ij} and R_y^{ij}, [10], [16], as follows

$$J_x \approx J_x^a = \sum_{i=1}^{N_x-1} \sum_{j=1}^{N_y} J_x^D(i,j)\, R_x^{i,j}(r) \qquad (8.a)$$

$$J_y \approx J_y^a = \sum_{i=1}^{N_x} \sum_{j=1}^{N_y-1} J_y^D(i,j)\, R_y^{i,j}(r) \qquad (8.b)$$

where $J^D = J_x^D\hat{x} + J_y^D\hat{y}$ is a discrete vectorial function. The rooftop functions extend over small rectangles of area $\Delta x\Delta y = (L_x/N_x)(L_y/N_y)$ and have their centers located at the points

$$r_x^{ij} = x_x^i\,\hat{x} + y_x^j\,\hat{y} = i\Delta\,\hat{x} + (j-.5)\Delta y\,\hat{y} \quad \text{for } R_x^{ij} \qquad (9.a)$$

$$r_y^{ij} = x_y^i\,\hat{x} + y_y^j\,\hat{y} = (i-.5)\Delta x\,\hat{x} + j\Delta y\,\hat{y} \quad \text{for } R_y^{ij} \qquad (9.b)$$

Fig. 8.3 shows the centers of the rooftops for the x and y-components.

The fields in (4) are smoothed using "razor-blade" functions, B_x and B_y for the x and y components respectively. Function B_x is defined as

$$B_x \begin{cases} 1 & \text{for } \begin{cases} |x| \le \Delta x/2 \\ y = 0 \end{cases} \\ 0 & \text{elsewhere} \end{cases} \qquad (10)$$

Function B_y is defined in a similar way, interchanging x and y in (10).

Discrete functions are obtained from the impressed and scattered fields by first performing a convolution of these fields with B_x or B_y and then sampling at discrete points using a train of delta functions. For instance for the impressed field component E_α^i (α equal to x or y) we have

$$E_\alpha^{iD}(r) = \text{Ш}(r_\alpha^{mn}) \int_{S_p} E_\alpha^i(r')B_\alpha(r-r')ds' \qquad (11)$$

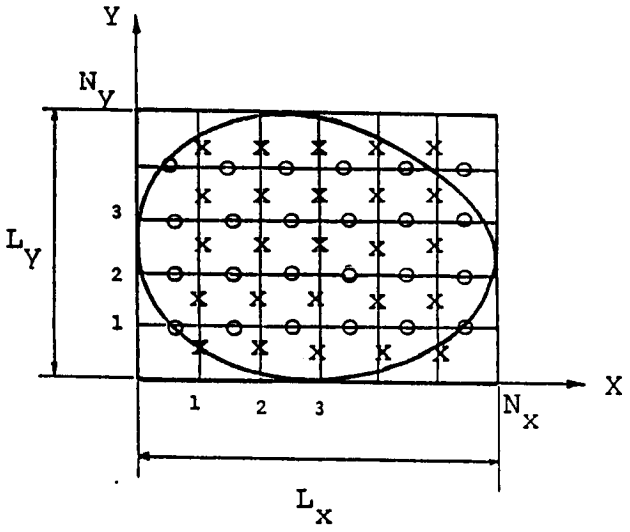

Figure 8.3 Rooftops centers for the $x(y)$ current component are indicated by crosses (circles).

where $\amalg(r_\alpha^{mn})$ represents the two dimensional sampling function

$$\amalg(r_\alpha^{mn}) = \sum_{m=-\infty}^{\infty} \sum_{n=-\infty}^{\infty} \delta(x - x_\alpha^m)\, \delta(y - y_\alpha^m) \tag{12}$$

where δ indicates the impulse function and r_α^{mn} is the center point of the rooftop R_α^{mn}.

With this procedure the following discrete equations can be obtained from (4).

$$E_x^{iD}(r) = -E_{xx}^{SD}(r) - E_{xy}^{SD}(r) \tag{13.a}$$

$$E_y^{iD}(r) = -E_{yx}^{SD}(r) - E_{yy}^{SD}(r) \quad \text{for } r \epsilon S_p \tag{13.b}$$

where

$$E_{\alpha\beta}^{SD} = -\amalg(r_\alpha^{mn}) \{\beta_\alpha \otimes G_{\alpha\beta}^F \otimes J_\beta^a\} \tag{14}$$

The symbol $\otimes$ indicates convolution and $G_{\alpha\beta}^F$ is one of the terms of the dyadic G^F

$$G^f = \begin{bmatrix} G_{xx}^F & G_{xy}^F \\ G_{yx}^F & G_{yy}^F \end{bmatrix} \tag{15}$$

8.4 Computation of the Integrals using FFT

The convolutions of (14) can be computed efficiently using the FFT. Here the procedure is shown for E_{xx}^{SD} and E_{xy}^{SD}. The procedure for E_{yx}^{SD} and E_{yy}^{SD} is similar.

a) Computations with E_{xx}^{SD}

To compute E_{xx}^{SD} a new coordinate system is considered. Calling x' and y' the coordinates in the system defined in Fig. 8.3, the new coordinates x and y are defined as follows (Fig. 8.4)

$$x = x' - \Delta x \tag{16.a}$$

$$y = y' - \Delta y/2 \tag{16.b}$$

E_{xx}^{SD} can be computed as

$$E_{xx}^{SD} = \frac{1}{(2\pi)^2} F^{-1}\left\{F[\text{Ш}(r_x^{mn})] \otimes \overline{E}_{xx}^{Sa}\right\} \tag{17}$$

where

$$r^{mn} = x^m\,\hat{x} + y^n\,\hat{y} = m\Delta\,\hat{x} + n\Delta\,\hat{y} \tag{18}$$

and $F(F^{-1})$ indicates direct (inverse) continuous Fourier Transform, ($\overline{\text{A}}$ stands for F(A)).

$$F(f(r)) = \int_{-\infty}^{\infty}\int_{-\infty}^{\infty} f(r)\, e^{-jk_x x}\, e^{-jk_y y}\, dxdy \tag{19}$$

So

$$\overline{E}_{xx}^{Sa}(k) = F\left\{B_x \otimes G_{xx}^{F} \otimes J_x^a\right\} = \overline{B}_x\,\overline{G}_{xx}^{F}\,\overline{J}_x^a \tag{20}$$

Using the properties of the sampling functions Ш, [17], [18], the convolution of (17) can be computed as

$$\overline{E}_{xx}^{eD}(k) = \frac{1}{\Delta x \Delta y} \sum_{m'=-\infty}^{\infty}\sum_{n'=-\infty}^{\infty} \overline{E}_{xx}^{Sa}(k_x - m'T_x^k,\, k_y - n'T_y^k) \tag{21}$$

where $T_x^k = 2\pi/\Delta x$ and $T_y^k = 2\pi/\Delta y$.

The functions that appear on the right side of (20) can be computed as follows

$$\overline{B}_x(k_x) = \Delta x\ sinc(k_x \Delta x/2) \tag{22}$$

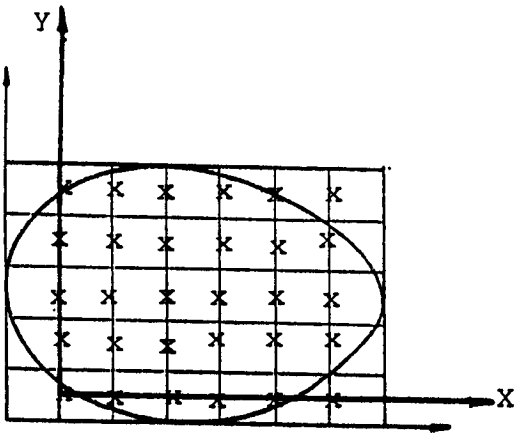

Figure 8.4 Coordinate system considered for the E_{xx}^{SD} computation.

$\overline{G}_{xx}^{F}$ can be obtained expressing G^F given in (5) as

$$G_{xx}^{F}(r) = \text{Ш}(v^{mn}) \otimes G_{xx}^{W}(r) \tag{23}$$

The Fourier Transform of G^F can be written now as

$$\overline{G}_{xx}^{F}(k) = \frac{(2\pi)^2}{T_x T_y} \text{Ш}(k^{mn}) \overline{G}_{xx}^{w}(k) \tag{24}$$

where

$$\begin{aligned} k^{mn} = k_x^m \, \hat{x} + k_y^n \, \hat{y} &= (2\pi m/T_x) \, \hat{x} + (2\pi n/T_y) \, \hat{y} \\ &= m(T_x^k/N_x^t) \, \hat{x} + n(T_y^k/N_y^t) \, \hat{y} \end{aligned} \tag{25}$$

where $N_x^t = 2N_x$ and $N_y^t = 2N_y$.

Having into account the expression (3) we can write $\overline{G}_{xx}^{w}$ as

$$\overline{G}_{xx}^{w}(k) = (2\pi)^2 \overline{Z}(k) \otimes \overline{G}_{xx}(k) \tag{26}$$

Analytical expressions for $\overline{G}_{xx}(k)$ can be obtained easily using the techniques described in [3] and [14]-[15]. Expressions for the Fourier Transform of some space-limited functions considered for Z are included in the table. It can be noticed that $\overline{G}_{xx}^{F}$ vanishes at all the

spectral points except at $k = k^{mn}$, so to compute $\overline{E}_{xx}^{Sa}$ in (20) we only need to compute $\overline{J}_x^a$ for these points. It can be found that

$$\overline{J}_x^a(k^{mn}) = \overline{R}_x(k^{mn})\overline{\overline{J}}_x^d(m,n) \tag{27}$$

where

$$\overline{R}_x(k) = \Delta x \Delta y \; sinc^2(k_x \Delta x/2) \; sinc(k_y \Delta y/2) \tag{28}$$

$$\begin{aligned}\overline{\overline{J}}_x^D(m,n) &= \sum_{i=0}^{N_x^t-1}\sum_{j=0}^{N_y^t-1} J_x^D(i,j)\exp(-j(k_x^m i\Delta x + k_y^n j\Delta y)) \\ &= N_x^t N_y^t \; FFT(J_x^D(i+1,j+1))\end{aligned} \tag{29}$$

FFT indicates Fast Fourier Transform with a period of size (N_x^t, N_y^t).

$\overline{E}_{xx}^{Sa}(k)$ can be written in a compact form

$$\overline{E}_{xx}^{Sa}(k) = \sum_{m=-\infty}^{\infty}\sum_{n=-\infty}^{\infty} \delta(k_x - k_x^m)\delta(k_y - k_y^n) W_{xx}^a(m,n)\overline{\overline{J}}_x^D(m,n) \tag{30}$$

where

$$W_{xx}^a(m,n) = (2\pi)^2 \Delta x \; \mathrm{sinc}^3(k_x^m \Delta x/2)\mathrm{sinc}(k_y^n \Delta y/2) G_{xx}^w(k^{mn}) \tag{31}$$

Combining (21) and (29)-(31) and taking into account the periodicity of $\overline{\overline{J}}_x^D$ we have

$$\overline{E}_{xx}^{SD}(k) = \frac{1}{\Delta x \, \Delta y}\sum_{m=-\infty}^{\infty}\sum_{n=-\infty}^{\infty} \delta(k_x - k_x^m)\delta(k_y - k_y^n) W_{xx}^a(m,n)\overline{\overline{J}}_x^D(m,n) \tag{32}$$

where W_{xx}^P is a discrete periodic function with the same period that $\overline{\overline{J}}_x^D$.

$$W_{xx}^P = \sum_{s=-\infty}^{\infty}\sum_{z=-\infty}^{\infty} W_{xx}^a(m - sN_x^t, n - zN_y^t) \tag{33}$$

Now E_{xx}^{SD} can be computed accurately for $r \epsilon S_p$, performing the inverse continuous Fourier Transform of (32) with the help of the FFT

$$E_{xx}^{SD}(r) = \frac{1}{(2\pi)^2}\sum_{m=0}^{Nx-1}\sum_{n=0}^{N_y-1} \delta(x - x^m)\delta(y - y^n) \; FFT^{-1}(W_{xx}^P \overline{\overline{J}}_x^D) \tag{34}$$

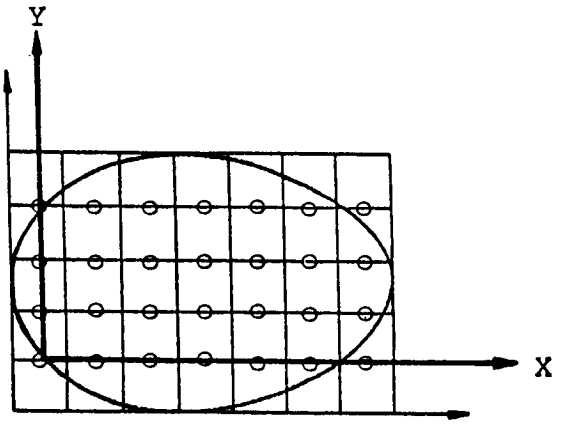

Figure 8.5 Coordinate system considered for the E_{xy}^{SD} computation.

where FFT^{-1} indicates inverse FFT with a period of size (N_x^t, N_y^t). It can be noticed that the values of E_{xx}^{SD} are obtained efficiently by using only two FFT's : a direct one in (29) and an inverse one in (34).

b) Computations with E_{xy}^{SD}

In this case we define another coordinate system (Fig. 8.5) :

$$x = x' - \Delta x/2 \tag{35.a}$$

$$y = y' - \Delta y \tag{35.b}$$

where x' and y' are the coordinates of Fig. 8.3

Now E_{xy}^{SD} can be computed using

$$\overline{E}_{xy}^{SD}(r) = \frac{1}{(2\pi)^2} F^{-1}\left\{F[\text{Ш}(r^{mn} - \overline{d})] \otimes \overline{E}_{xy}^{Sa}\right\} \tag{36}$$

where

$$\overline{d} = (\Delta x/2)\hat{x} - (\Delta y/2)\hat{y} \tag{37}$$

$$\overline{E}_{xy}^{Sa}(k) = \overline{B}_x\, \overline{G}_{xy}^{F}\, \overline{J}_y^a \tag{38}$$

The Fourier Transform of the shifted sampling function of (36) can be written as

$$F(\text{Ш}(r^{mn} - \overline{d})) = \frac{1}{\Delta x \Delta y} \sum_{m'=-\infty}^{\infty} \sum_{n'=-\infty}^{\infty} (-1)^{-m'}(-1)^{-n'}\, \delta(k_x - m'T_x^k)\, \delta(k_y - n'T_y^k) \tag{39}$$

and therefore for $\overline{E}_{xy}^{SD}$ we have

$$\overline{E}_{xy}^{SD}(k) = \frac{1}{\Delta x \Delta y} \sum_{m'=-\infty}^{\infty} \sum_{n'=-\infty}^{\infty} (-1)^{-m'}(-1)^{-n'} \overline{E}_{xy}^{Sa}(k_x - m'T_x^k, k_y - n'T_y^k) \quad (40)$$

Using a development similar to (22)-(29) the following expression for $\overline{E}_{xy}^{Sa}$ can be found

$$\overline{E}_{xy}^{Sa}(k) = \sum_{m=-\infty}^{\infty} \sum_{n=-\infty}^{\infty} \delta(k_x - k^m)\delta(k_y - k^n) W_{xy}^a(m,n) \overline{\overline{J}}_y^D(m,n) \quad (41)$$

where

$$W_{xy}^a(m,n) = (2\pi)^2 \Delta x \mathrm{sinc}^2(k_x^m \Delta x/2)\mathrm{sinc}^2(k_y^n \Delta y/2)\overline{G}_{xy}^w(k^{mn}) \quad (42)$$

Combining now (40) and (41) and taking into account the periodicity of $\overline{\overline{J}}_y^D$ we can obtain

$$\overline{E}_{xy}^{SD}(k) = \frac{1}{\Delta x\, \Delta y} \sum_{m=-\infty}^{\infty} \sum_{n=-\infty}^{\infty} [\delta(k_x - k_x^m) exp(-j\Delta x k_x/2)] [\delta(k_y - k_y^n) exp(+j\Delta y k_y/2)] W_{xy}^P(m,n) \overline{\overline{J}}_y(m,n) \quad (43)$$

where $\overline{\overline{J}}_y$ and W_{xy}^P are discrete periodic functions with period of size (N_x^t, N_y^t). W_{xy}^P is defined as follows

$$W_{xy}^P = exp(+jk_x^m \Delta x/2) exp(-jk_y^n \Delta y/2) \sum_{s=-\infty}^{\infty} \sum_{z=-\infty}^{\infty} (-1)^{-s}(-1)^{-z} W_{xy}^a(m - sN_x^t, n - zN_y^t) \quad (44)$$

Now for $r \epsilon S_p, E_{xy}^{SD}$ can be computed accurately performing the inverse continuous Fourier Transform of (43) using the inverse FFT as shown in the following expression

$$E_{xy}^{SD}(r) = \frac{1}{(2\pi)^2} \sum_{m=0}^{N_x-1} \sum_{n=0}^{N_y-1} \delta(x - (x^m + \Delta x/2))\delta(y - (y^n - \Delta y/2)) FFT^{-1}(W_{xy}^P \overline{\overline{J}}_y^D) \quad (45)$$

E_{xy}^{SD} is obtained using only two FFT's : a direct one for $\overline{\overline{J}}_y^D$ and the inverse one of (45).

It can be noticed from the definitions of the coordinate systems considered for E_{xx}^{SD} and E_{xy}^{SD} (equations (16) and (35) respectively) that these fields are given by a series of delta functions with impulse responses in the center-point of rooftops R_{mn}^x, in accordance with the definitions of these fields given in (14).

A discussion about the computation of the series of (33) and (44) is given in [13], where it is found that good approximations with a minimum of ripple problems can be obtained by considering only the first four terms of the series. Thus we only need to consider the terms with s=0,-1 and z=0,-1. All the results presented here have been obtained using these four terms.

Now all the steps for the computation of the direct discrete operator have been given except for the evaluation in the spectral domain of the modified Green's function, G^F.

8.5 Modified Green's Function Computation

Using the present CG-FFT scheme each one of the four terms of the dyadic $\overline{G}^F$ must be computed for the discrete points k^{mn}, defined in (25). For $\overline{G}_{\alpha\beta}^F$ we have

$$\overline{G}_{\alpha\beta}^F(k^{mn}) = \frac{(2\pi)^2}{T_x T_y} \int_{-S_y}^{S_y} dk_y \int_{-S_x}^{S_x} \overline{G}_{\alpha\beta}(k^{mn} - k)\overline{Z}(k)dk_x \qquad (46)$$

where $(-S_x, S_x)$ and $(-S_y, S_y)$ represent the spectral band over which $\overline{Z}$ do not vanish.

In this work $\overline{Z}$ is restricted to be the product of a pair of functions of a single variable

$$\overline{Z}(k) = \overline{Z}_x(k_x)\overline{Z}_y(k_y) \qquad (47)$$

In the real domain Z_x and Z_y must be band-limited functions, (Z must vanish for $|x| > L_x$ and $|y| > L_y$, as explained in Part II). Therefore $\overline{Z}_x$ and $\overline{Z}_y$ extend over all the spectral domain and integral (46) must be performed for $S_x \to \infty$ and $S_y \to \infty$. However, for the sake of numerical efficiency some truncations in these limits must be considered.

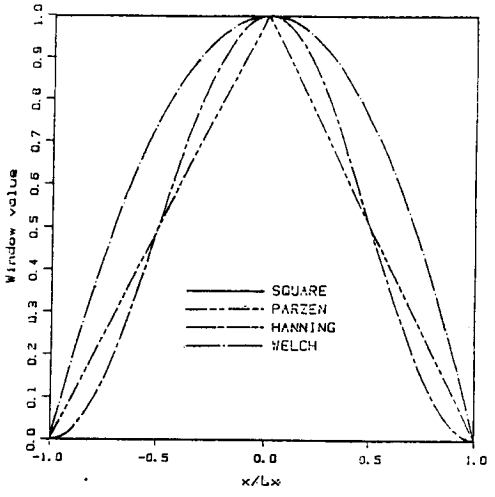

Figure 8.6 Real domain picture of the window functions of the table.

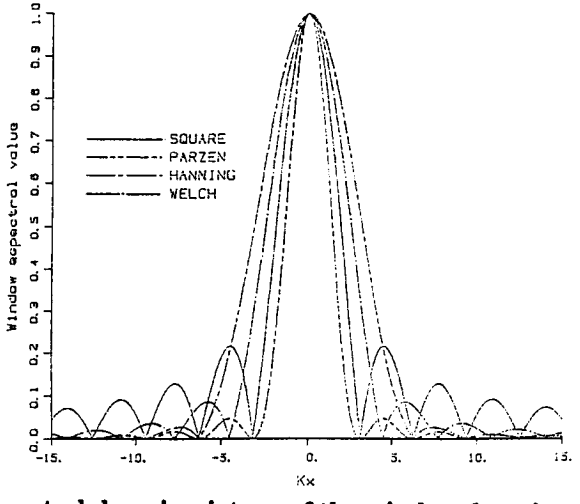

Figure 8.7 Spectral domain picture of the window functions of the table.

For Z_x and Z_y well known window functions are available, [19]. Four of them are defined in the table. Pictures of these four window functions are shown in Figs. 8.6 and 8.7 for the real and spectral domain, respectively. In the spectral domain they have a well defined main lobe and a set of decreasing minor lobes. Using a Pulse window, Eqs. (2) and (4) have exactly the same solution but this function has in the spectral domain very slowly decreasing lobes that do not make it feasible to perform a large truncation in the integrals limits of (46).

The Triangle window has very fast decreasing lobes but in this case G^w and G are very different and Eqs. (2) and (4) would not have similar solutions. Hanning and Welch's windows represent a trade off between functions that have fast decreasing secondary lobes and functions that make it feasible that G^w and G to be reasonably equal over nearly all the points where these windows do not vanish. Using these windows the integral of (46) can be performed with enough accuracy considering for $\overline{Z}_x$ and $\overline{Z}_y$ only their main lobe. Authors have done some numerical experimentation with these windows, studying parameters such as: 1) the agreement of the CG-FFT results with reliable solutions, 2) the convergence rate of the solution, 3) the stability of the solution with the number of samples considered to represent the current 4) and the CPU time. The best results have been obtained using Welch's window for Z_x and Z_y and considering only the main lobe. Gauss's quadrature rule has been used to compute (46) considering 2x2, 8x8 and 32x32 quadrature points when the singularities of $\overline{G}_{\alpha\beta}$ are far away from, close and within the integration band, respectively.

8.6 Results

Results for conducting plates in free space obtained by other methods or measurements can be useful to validate the proposed CG-FFT scheme. Fig. 8.8 shows two current distribution cuts for a square conducting plate, in free space. A plane wave is normally incident on the plate. A comparison with the MM results that appear in [20] is made. An excellent agreement between CG-FFT and MM results can be noticed. Results with both methods have been obtained using a similar number of samples.

A study of the stability of the current distribution results when the number of samples is increased is made in Figs. 8.9-8.10 for the square conducting plate problem of Fig. 8.8. A high degree of stability for the current cut curves can be observed, except for the points near the edges of the plates. In these points the asymptotic edge behavior of the current is best obtained when the number of samples is increased, as could be expected. It can be also noticed that the ripple for the BB' cut is very small. No ripple can be observed in the other cut.

Figures 8.11-8.12 show data for the bistatic RCS at normal incidence of a perfectly conducting disk in free space. A comparison is

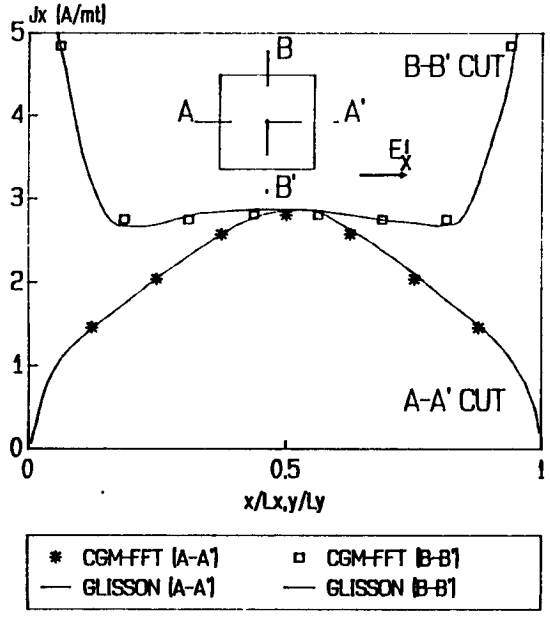

Figure 8.8 Amplitude of the co-polar surface current on a 1. λ square plate illuminated by a plane wave as shown. CG-FFT method is applied using $7\times8 = 56$ basis functions to represent each component of the current (J_x and J_y).

made with analytical results obtained by Hodge, [21]. These analytical results are very reliable and can be used for validation purposes of numerical methods or measurements facilities. It can be observed that the CG-FFT and Hodge's results are very close, even for directions far from the disk normal.

Current distribution cuts for a rectangular microstrip patch are shown in Fig. 8.13. A plane wave is normally incident on the patch. Two cuts are given for the co-polar component of the current. The shapes of the cuts indicate that the computed induced equivalent current satisfies the asymptotic edge form. The curves appear without ripple and due to current expansion considered, (8), the current vanishes for points outside the patch. These last two features of the current behavior were not obtained in [3].

RCS data for two problems with a microstrip patch are given in Figs. 8.14-8.15. CG-FFT results are compared with the numerical or measured values that appear in [22]-[23]. The measurements of Fig. 8.14 were performed using a finite rectangular substrate. In the present CG-

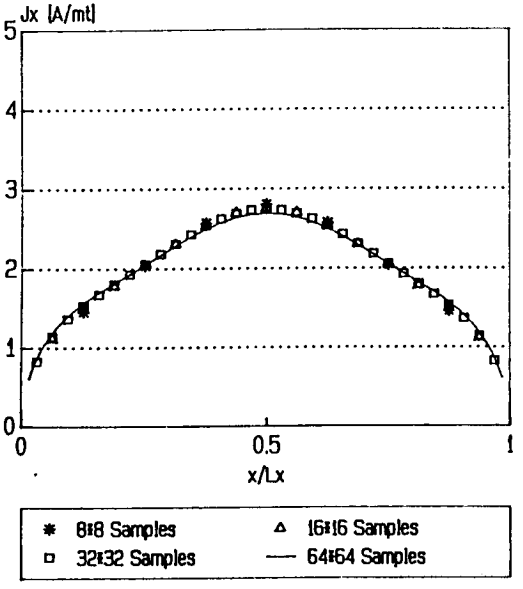

Figure 8.9 Results of a convergence study for the x component of the current for the AA' cut in Fig. 8.8.

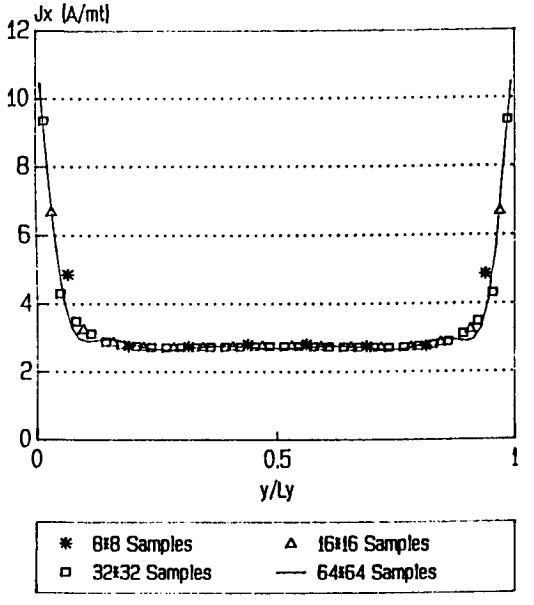

Figure 8.10 Results of a convergence study for the x component of the current for the BB' cut in Fig. 8.8.

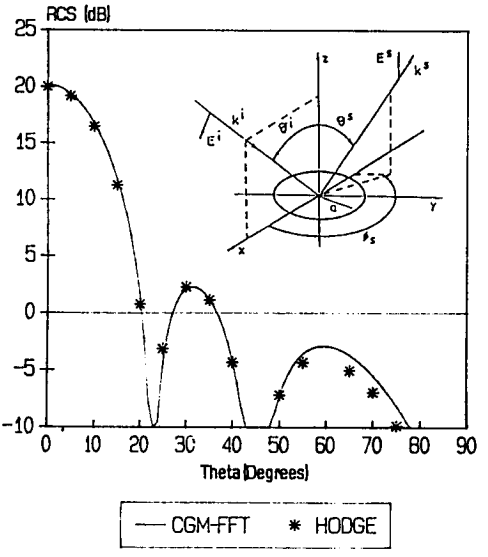

Figure 8.11 Bistatic RCS of a disk. E-plane cut, (normal incidence, ka = 10.)

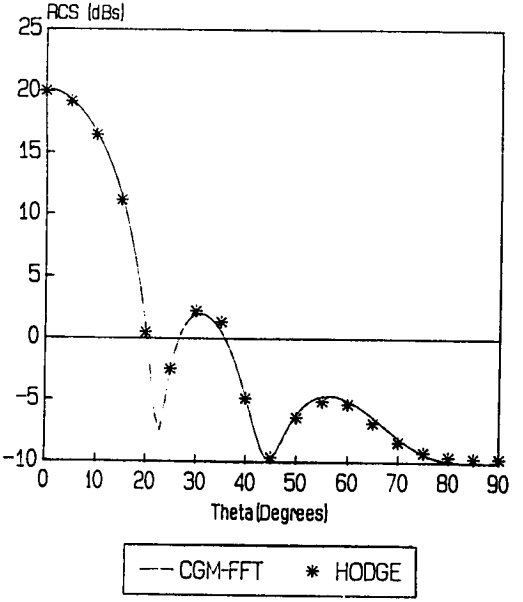

Figure 8.12 H-plane cut for the problem indicated in Fig. 8.11.

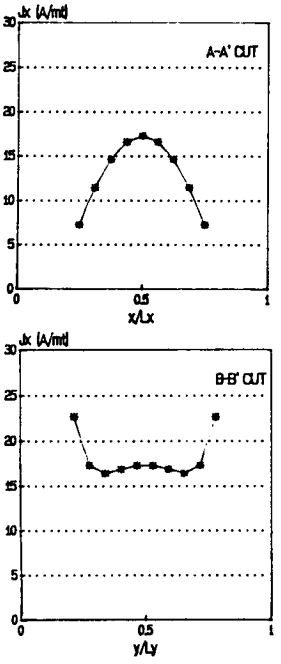

Figure 8.13 Amplitude of the co-polar surface current of a rectangular microstrip patch, (L = 1. cm, W = 1.5 cm), illuminated by a x-polarized plane wave, (f=3.12 GHz). The substrate has a width d = .127 cm, a permittivity ϵr = 10.2. The number of samples considered to represent each current component is 9×10 (see sketch in Fig. 8.14).

FFT approach the patches are considered lying over infinite substrates. It can be noticed that the agreement between numerical and measured data is within the limits of experimental error and that in all the curves the resonance frequencies are obtained nearly for the same values.

Finally, Figs. 8.16-8.17 show curves for the evolution of the relative error versus the number of iterations for the problems indicated in Figs. 8.8 and 8.13, respectively. The relative error is defined as

$$e_r = 10 \log \frac{|LI - Y|}{|Y|}(dB) \tag{48}$$

where $|A|$ represents the norm of A.

All the results of Figs. 8.8-8.15 were obtained with a relative error less or equal than -20 (dB)

The shape of the curves of Figs. 8.16-8.17 shows the typical behavior for the convergence rate observed by the authors in all their numerical experimentation. From this experience and for problems of

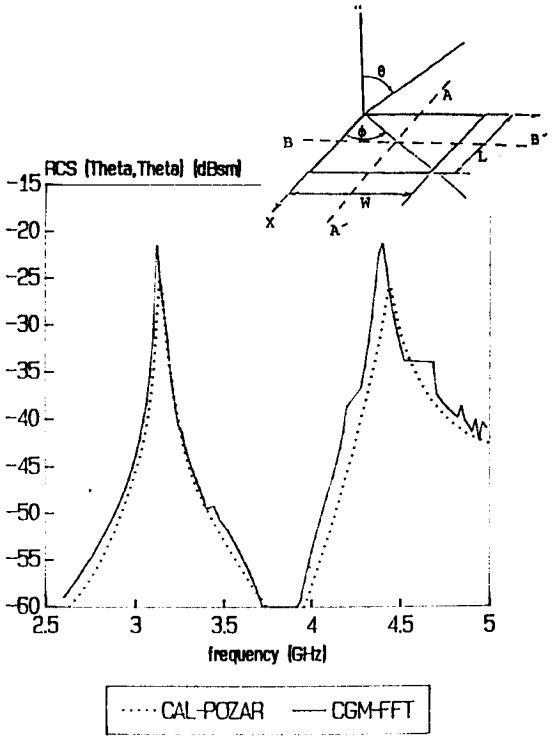

Figure 8.14 $\theta - \theta$ Backscatter RCS data for the rectangular microstrip patch indicated ($L = 1.cm, W = 1.5cm, d = .127cm, \epsilon r = 10.2, \theta = 0°, \phi = 45°$). CG-FFT method is applied using 9×10 basis functions to represent each component of the current.

resonant size, it can be said that the number of iterations, N_i, required to obtain a fixed relative error is approximately proportional to the squared root of number of subdomains considered, $(N_x N_y)^{1/2}$. The computation time per iteration is proportional to $N_x N_y log(N_x N_y)$. The total CPU time, t, to solve a problem with a fixed relative error follows the rule $t = C(N_x N_y)^{3/2} log(N_x N_y)$, where C is a constant. On the other hand, the memory requirements for the CG-FFT method is only several vectors of dimension $4N_x N_y$. These figures for the CPU-time and memory requirement indicate that the proposed CG-FFT scheme is highly efficient for the analysis of arbitrary patches in multilayer media.

All the CG-FFT results have been obtained using a FPS-164 Array Processor attached to a VAX/750. This processor has a word length of 64 bits and the theoretical speed of this system is about 11 Mflops.

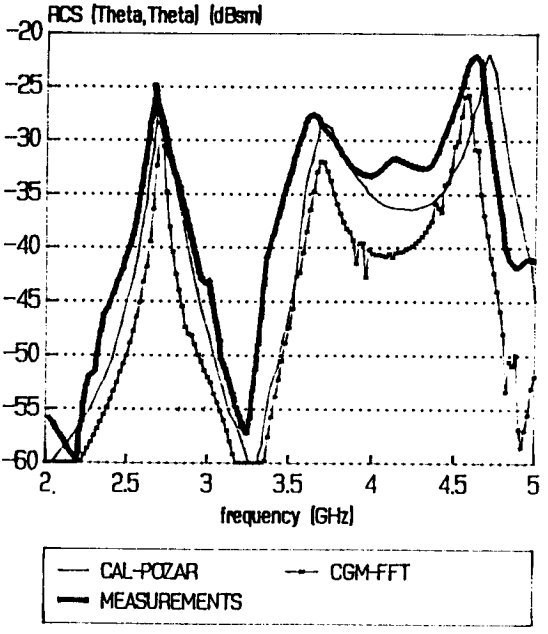

Figure 8.15 $\theta - \theta$ **Backscatter RCS data for the rectangular microstrip patch indicated** ($L = 3.66cm, W = 2.6cm, d = .158cm, \epsilon r = 2.17, \theta = 60°, \phi = 45°$). **CG-FFT method is applied using 9×10 basis functions to represent each component of the current.**

The CPU-time to solve the problems indicated in Figs 8.14-8.15 was about one minute for each frequency.

8.7 Conclusions

An efficient CG-FFT scheme to analyze finite conducting plates of arbitrary geometry in multilayer media has been described. Nearly all the computations are performed in the spectral domain. A modified Green's function is introduced and sampled in the spectral domain. This function is obtained from the well known expressions of Green's functions in the spectral domain and therefore the CG-FFT scheme can be used to analyze any multilayer media configuration. The scheme can be easily modified to analyze periodic structures by suppressing the windowing of Green's function. An extension of the work to be considered for the future is to particularize the scheme to solve the problem using MPIE, [24]-[26]

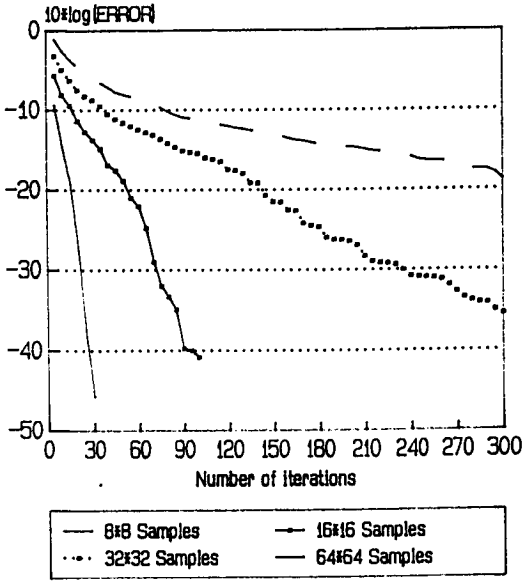

Figure 8.16 Results of a convergence study of the relative error for the problem of Fig. 8.8.

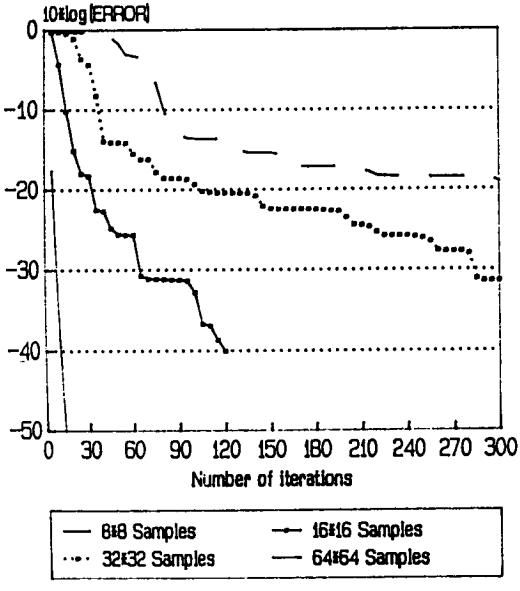

Figure 8.17 Results of a convergence study of the relative error for the problem of Fig. 8.13.

Appendix

Complete expressions to compute the scattered field with the direct and adjoint operator and to compute the inner products are shown here.

The scattered fields E_x^{SD}, E_y^{SD} given in (14), can be expressed as

$$E_\alpha^{SD} = \sum_{m=1}^{N_x} \sum_{n=1}^{N_y} \delta(x - x_\alpha^m)\, \delta(y - y_\alpha^n)\, E_\alpha^\delta(m-1, n-1) \qquad (A.1)$$

where $\alpha = x$ or y and E_α^δ is a discrete function that can be computed as follows

$$\begin{bmatrix} E_x^\delta \\ E_y^\delta \end{bmatrix} = C_e\, F^{-1} \begin{bmatrix} W_{xx}^P & W_{xy}^P \\ W_{yx}^P & W_{yy}^P \end{bmatrix} \times \begin{bmatrix} F(J_x^D(i+1, j+1)) \\ F(J_y^D(i+1, j+1)) \end{bmatrix} \qquad (A.2)$$

where $F(F^{-1})$ is the direct (inverse) Fast Fourier Transform, and

$$C_e = \frac{N_x^t\, N_y^t}{(2\pi)^2} \qquad (A.3)$$

$W_{\alpha\beta}^P$ is given in (33) and (44) for $\alpha\beta = xx$ and $\alpha\beta = xy$, respectively. J_x^D, J_y^D are given in (8.a) and (8.b).

The inner product computations required in the CGM algorithm can be evaluated as follows

$$\begin{aligned} < J^a, E(J^b) > &= < J_x^a, E_x(J^b) > + < J_y^a, E_y(J^b) > \\ &= < J_x^a, E_x^b > + < J_y^a, E_y^b > \end{aligned} \qquad (A.4)$$

where, for instance, the scalar inner product of J_x^a and E_x^b is

$$\begin{aligned} < J^a, E_x^b > = \int_{S_p} J_x^a (E_x^b)^* = \int \Bigg[\sum_{i=1}^{Nx-1} \sum_{j=1}^{Ny} J_x^{aD}(i,j)\, R_x^{ij}(r) \Bigg] \\ \Bigg[\sum_{i'=1}^{Nx} \sum_{j'=1}^{Ny} \delta(x - x_\alpha^{i'})\, \delta(y - y_\alpha^{i'})\, E_x^{b\delta *}(i'-1, j'-1) \Bigg] \\ ds = \sum_{i=1}^{Nx-1} \sum_{j=1}^{Ny} J_x^{aD}(i,j)\, E_x^{b\delta *}(i-1, j-1) \end{aligned} \qquad (A.5)$$

where J_x^{aD} and $E_x^{b\delta}$ are discrete functions obtained by expanding J_x^a and E_x^b, as it is shown in (8) and in (A.1) respectively.

It can be obtained that the computations with the adjoint operator can be performed by using

$$\begin{bmatrix} E_x^{\delta,adj} \\ E_y^{\delta,ddj} \end{bmatrix} = C_e\, F^{-1} \begin{bmatrix} W_{xx}^{P*} & W_{yx}^{P*} \\ W_{xy}^{P*} & W_{yy}^{P*} \end{bmatrix} \times \begin{bmatrix} F(J_x^D(i+1,j+1)) \\ F(J_y^D(i+1,j+1)) \end{bmatrix} \quad (A.6)$$

where $E_\alpha^{\delta,adj}$ means the adjoint of E_α^δ.

References

[1] Pozar, D. M., "An update on microstrip antenna theory and design including some novel feeding techniques," *IEEE Antennas and Propag. Society Newsletter,* 5–9, October 1986.

[2] Jansen, R. H., R. G. Arnold, and I. G. Edison, "A compresive CAD approach to the design of MMIC's up to MM-wave frequencies," *IEEE Transac. Microwaves Theory Tech,* **MTT-36,** 208–219, 1988.

[3] Kastner, R., E. Heyman, and A. Sabban, "Spectral domain iterative analysis of single and double-layered microstrip antennas using the Conjugate Gradient algorithm," *IEEE Transac. Antennas and Propag.,* **AP-36,** 1204–1212, 1988.

[4] Pozar, D. M. "Input impedance and mutual coupling of rectangular micro- strip antennas," *IEEE Transac. Antennas and Propag.,* **AP-30,** 1191–1196, 1982.

[5] Bailey, M. C., and M. D. Deshpande, "Analysis of elliptical and circular microstrip antennas using Moment Method," *IEEE Transac. Antennas and Propag.,* **AP-33,** 954–959, 1985.

[6] Mosig, J. R., "Arbitrarily shaped microstrip structures and their analysis with a mixed potential integral equation," *IEEE Transac. Microwaves Theory Tech.,* **MMT-36,** 314–323, 1988.

[7] Sarkar, T. K., and S. M. Rao, "The application of the Conjugate Gradient Method for the solution of electromagnetic scattering from arbitrarily oriented wire antennas," *IEEE Transac. on Antennas and Propag.,* **AP-32,** pp 398–403, 1984.

[8] Sarkar, T. K., and E. Arvas, "Application of FFT and the Conjugate Gradient method for the solution of electromagnetic radiation from electrically large and small conducting bodies," *IEEE Transac. Antennas and Propag.*, **AP-34**, 635–640, 1986.

[9] Peterson, A. F., "An analysis of the spectral iterative technique for electromagnetic scattering from individual and periodic structures," *Electromagnetics*, **6**, 255–276, 1986.

[10] Cátedra, M. F., J. G. Cuevas, and L. Nuño, "A scheme to analyze conducting plates of resonant size using the Conjugate-Gradient Method and the Fast Fourier Transform," *IEEE Transac. Antennas and Propag.*, **AP-36**, 1744–1752, 1988.

[11] Cátedra, M. F., E. Gago, and L. Nuño, "A numerical scheme to obtain the RCS of Three-dimensional bodies of resonant size using the Conjugate-Gradient Method and the Fast Fourier Transform," *IEEE Transac. Antennas and Propag.*, **AP-37**, No. 5, 528–537, May 1989.

[12] Cwik, T. A., and R. Mittra, "Scattering from a periodic array of free-standing arbitrarily shaped perfectly conducting or resistive patches," *IEEE Transac. Antennas and Propag.*, **AP-33**, 1226–1234, 1987.

[13] Cátedra, M. F., and R. P. Torres, "A scheme to analyze scattering from flat metallic periodic structures using the Conjugate-Gradient and the Fast Fourier Transform method," to appear in *Progress in Electromagnetics Research, PIER*, series book, Elsevier, 1990.

[14] Itoh, T., "Spectral domain immittance approach for dispersion characteristics of generalized printed transmission lines," *IEEE Transac. Microwaves Theory Tech.*, **MTT-28**, 733–736, 1980.

[15] Vegni, L., R. Ciccheti, and P. Capece, "Spectral dyadic Green's function formulation for planar integrated structures," *IEEE Transac. Antennas and Propag.*, **AP-36**, 1057–1065, 1988.

[16] Glisson, A. W., and D. R. Wilton, "Simple and efficient numerical methods for problems of electromagnetic radiation and scattering from surfaces," *IEEE Transac. Antennas and Propag.*, **AP-28**, 593–603, 1980.

[17] Elliott, D. F., and K. R. Rao, *Fast Transforms Algorithms, Analysis, Applications*, Academic Press, 1982.

[18] Bracewell, R. N., *The Fourier Transform and its applications*, Second Edition, McGraw-Hill, 1978.

[19] Press, W. H., B. P. Flannery, S.A. Teakolsky, and W. T. Vetterling, *Numerical recipes. The art of Scientific computing*, Cambridge University Press, Cambridge 1986.

[20] Rao, S. M., D. Wilton, and A. W. Glisson, "Electromagnetic scattering by surfaces of arbitrary shape," *IEEE Transac. Antennas and Propag.*, **AP-30**, 404–418, 1982.

[21] Hodge, D. B., "Scattering by a circular metallic disk," *IEEE Transac. Antennas and Propag.*, **AP-28**, 707–712, 1980.

[22] Newman, E. H., and D. Forral, "Scattering from a microstrip patch," *IEEE Transac. Antennas and Propag.*, **AP-35**, 245–251, 1987.

[23] Pozar, D. M., "Radiation and scattering from a microstrip patch on a uniaxial substrate," *IEEE Transac. Antennas and Propag.*, **AP-35**, 613–621, 1987.

[24] Michalski, K. A., "The mixed-potential electric field integral equation for objects in layered media," *Arch. Elek. Übertragung*, **39**, 317–322, Sept-Oct. 1985

[25] Michalski, K. A., "On the scalar potential of a point charge associated with a time-harmonic dipole problem," *IEEE Transac. Antennas and Propag.*, **AP-35**, 1299–1301, 1987.

[26] Michalski, K. A., and D. Zheng, "Electromagnetic scattering and radiation by surfaces of arbitrary shape in layered media, Part I: Theory," Submitted to *IEEE Transac. Antennas and Propag.*